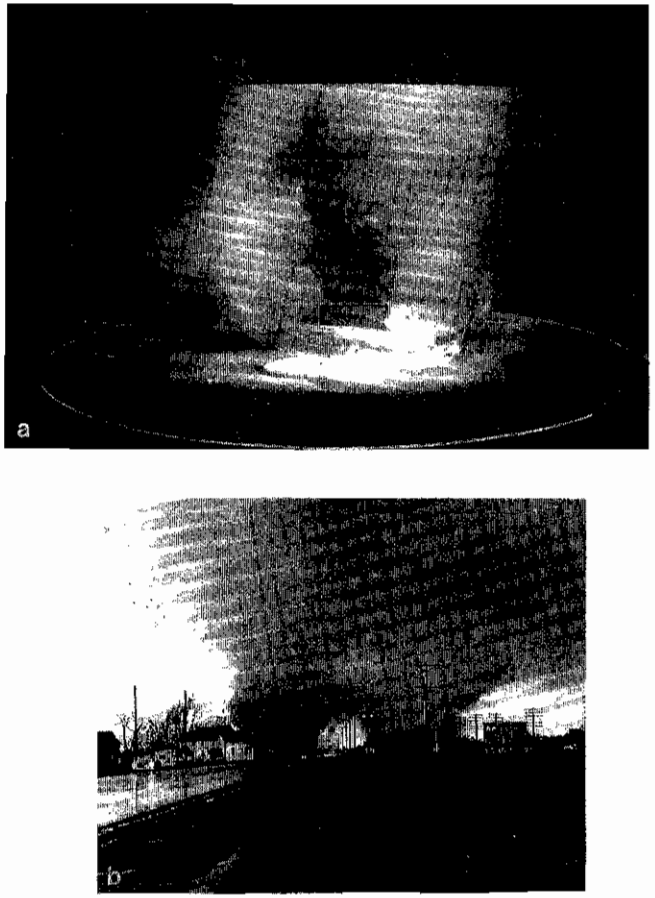

Figure 8.37 (a) Laboratory vortex pair compared with double tornado of 11 April 1965 at Elkhart, Indiana (b). (Laboratory example from Davies-Jones, 1986; tornado photo by Paul Huffman.)

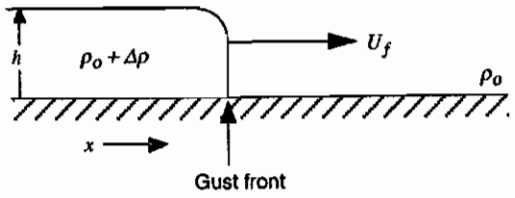

Figure 8.38 Gravity current of density $\rho_o + \Delta\rho$ and depth h moving through a fluid of density ρ_o at speed U_f in the x-direction.

8.9 Gust Fronts

The outflow of downdraft air from thunderstorms along the ground is a very important phenomenon. It can help to generate new thunderstorm cells, and it can cut old cells off from their supply of buoyant air. The boundary of the advancing outflow marks a major change in surface meteorological conditions and is thus of interest in forecasting and nowcasting. Damaging winds[229] often occur at this boundary, which is usually referred to as the *gust front*. In this section, we explore its dynamics.

The gust front is an example of the geophysical phenomenon called a *gravity current*, which may be defined as a mass of high-density fluid flowing along a horizontal bottom and displacing ambient fluid of lesser density.[230] Other examples include salt water intruding into a fresh water estuary, or muddy water displacing fresh water at the bottom of a lake. The gravity current is driven by the horizontal pressure gradient acting across the sharp lateral interface separating the two fluids. The physical situation is shown in idealized form in Fig. 8.38 for a gravity current moving at speed U_f in the x-direction. The role of the pressure gradient in determining the speed of the current can be seen from the x-component of the Boussinesq momentum equation (2.47) in the absence of friction or Coriolis forces:

$$\frac{Du}{Dt} = -\frac{1}{\rho_o}\frac{\partial p^*}{\partial x} \tag{8.39}$$

If this expression is applied to a steady-state horizontal flow in a coordinate system moving with the gust front, it may be written as

$$\frac{\partial\left(u^2/2\right)}{\partial x} = -\frac{1}{\rho_o}\frac{\partial p^*}{\partial x} \tag{8.40}$$

If the gravity current has depth h and density $\rho_o + \Delta\rho$, where $\Delta\rho > 0$, and is moving through a stagnant base-state environment, integration of (8.40) across the front edge of the gravity current gives us

$$\frac{U_f^2}{2} = g\frac{\Delta\rho}{\rho_o}h \tag{8.41}$$

Thus, the speed of the gust front is determined by the depth of the gravity current and the density difference across the interface.

A schematic cross section through the gust front of a thunderstorm is shown in Fig. 8.39. This sketch is a composite of information derived from a variety of sources, including instrumented towers, weather radar, cloud observations, and

[229] Sometimes called "straight-line winds."

[230] For an overview of gravity currents in earth and planetary sciences, see the book *Gravity Currents* by Simpson (1987).

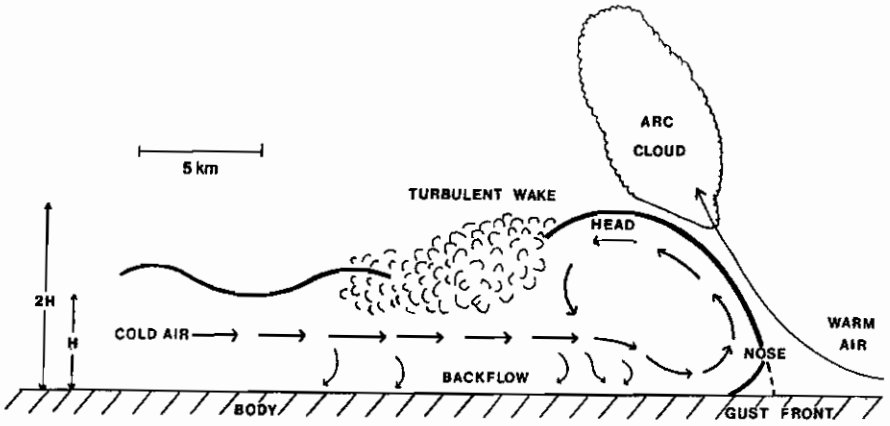

Figure 8.39 Schematic cross section through the gust front of a thunderstorm. (From Droegemeier and Wilhelmson, 1987; based on earlier studies of Charba, 1974; Goff, 1975; Wakimoto, 1982; Koch, 1984. Reprinted with permission from the American Meteorological Society.)

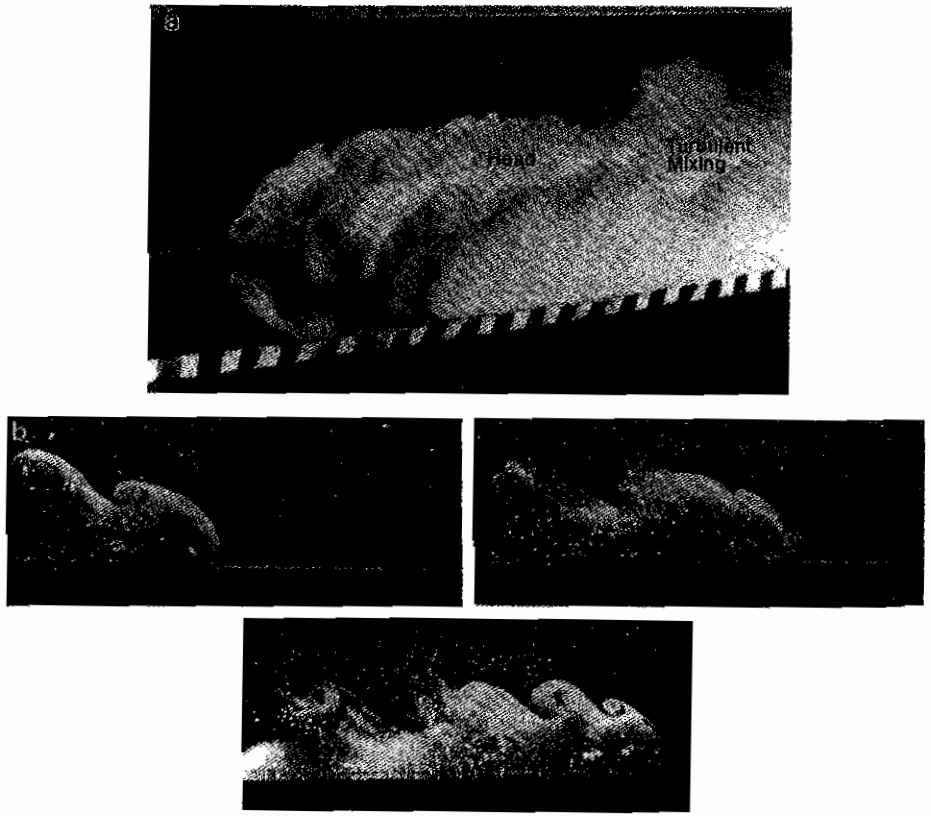

Figure 8.40 (a) and (b) Density currents observed in laboratory tanks. (From Simpson, 1969. Reprinted with permission from the Royal Meteorological Society.)

time series of surface meteorological data. The structure shown is remarkably similar to that of density currents observed in laboratory tanks (Fig. 8.40). Characteristic features include the bulbous *head* marking the leading portion of the current. Within the head is an overturning internal circulation. Following the head is a turbulent wake, which is, in turn, followed by several waves distorting the shape of the upper boundary of the dense outflow. An arc cloud sometimes forms in response to the lifting over the head.

Further details of the flow in thunderstorm outflows have been deduced from cloud models of the type discussed in Sec. 7.5.3. Results from a model simulation are shown in Figs. 8.41–8.44 .[231] A shallow layer of cold air moving along the ground enters a two-dimensional (x–z) model domain from the side. The inflow enters the domain with an assigned temperature profile, depth, and vertically averaged perturbation potential temperature. As the cold layer moves across the domain, the pressure perturbation at the surface is characterized by a high at its leading edge (Fig. 8.41a). This high reflects the peak of dynamic pressure produced at the leading edge. The maximum convergence coincides with the pressure maximum (Fig. 8.41b). From the momentum equation (8.39), we can see how this pressure perturbation is derived from the kinetic energy of the low-level relative flow toward the gust front, when it is stagnated by the wall of denser fluid. If we follow a parcel of fluid moving in the x-direction at horizontal velocity $u = Dx/Dt$, then we can make the transformation $1/Dt = u/Dx$ and (8.39) can be written as

$$\frac{D}{Dx}\left(\frac{u^2}{2} + \frac{p^*}{\rho_o}\right) = 0 \tag{8.42}$$

where Dx represents the distance between two successive locations of the fluid parcel. If this expression is integrated along the path of a parcel moving along the surface from some location far ahead of the gust front (where its relative motion is toward the gust front at speed U_f and the pressure perturbation is zero) to a point immediately ahead of the surface position of the gust front (where the relative motion of the parcel has been reduced to 0), then the pressure perturbation at the gust front is found to be

$$p^* = \rho_o \tfrac{1}{2} U_f^2 \tag{8.43}$$

Thus, the pressure perturbation at the surface at a point just ahead of the density current results from the conversion of horizontal kinetic energy to enthalpy (p^*/ρ_o). Since the stagnation occurs *ahead* of the leading edge of the gravity current, there is no hydrostatic contribution to p^* at this point.

The second maximum of pressure to the rear of the head is hydrostatic. It simply reflects the weight of the fluid above. The minimum of pressure separating the two highs is, however, nonhydrostatic. It is associated with rotation. As can be seen from Fig. 8.42, the low-pressure center in the middle of the head coincides with a center of rotation, which can be inferred from the horizontal and vertical

[231] These results are from a definitive paper by Droegemeier and Wilhelmson (1987).

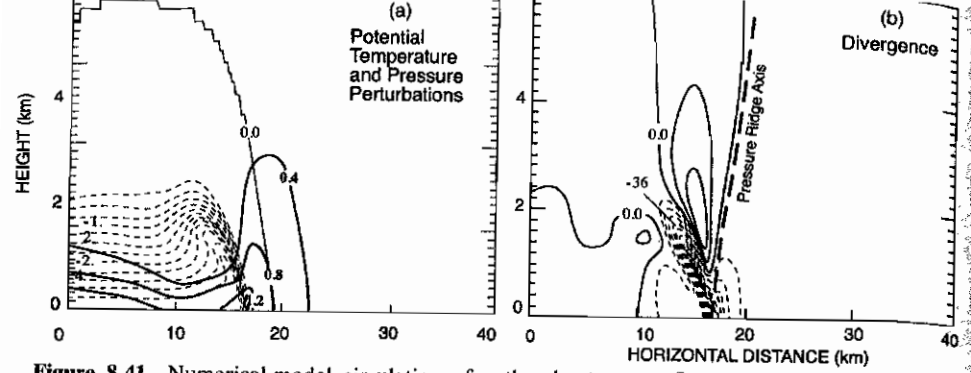

Figure 8.41 Numerical-model simulation of a thunderstorm outflow structure illustrating the nature of the surface pressure perturbation maxima associated with the outflows. (a) Potential temperature perturbation (K, thin contours, negative values dashed) and pressure perturbation (mb, heavy contours) show a maximum of pressure perturbation at the left-hand side of the domain which is hydrostatic. (b) Horizontal divergence (units of 10^{-4} s^{-1}, negative values dashed). (From Droegemeier and Wilhelmson, 1987. Reprinted with permission from the American Meteorological Society.)

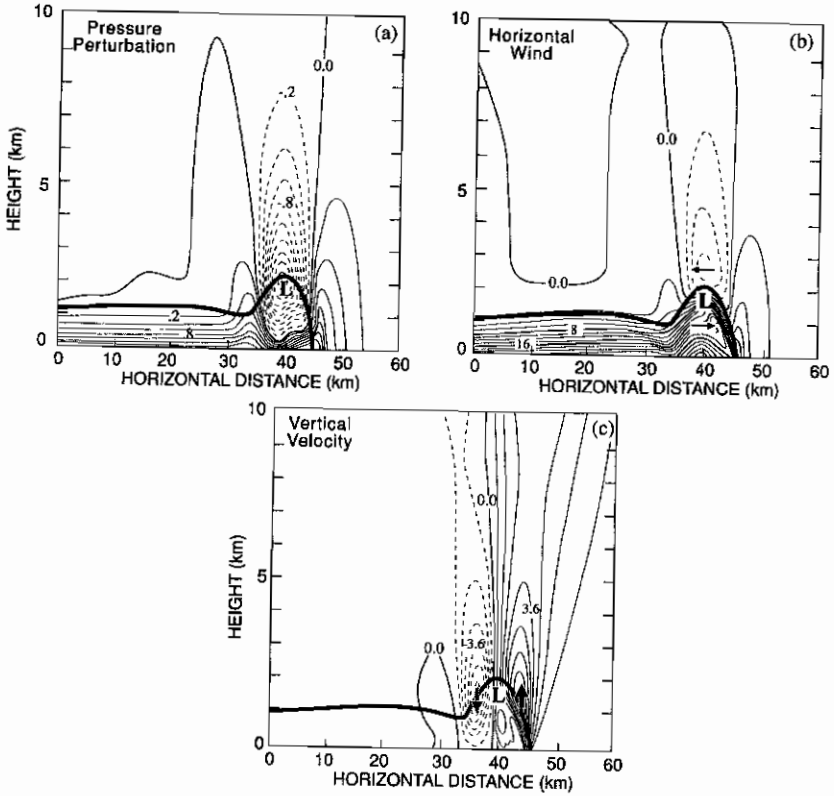

Figure 8.42 Numerical-model simulation of a thunderstorm outflow structure illustrating the ressure perturbation minimum and associated airflow in the head of the gust-front outflow. (a) 'ressure perturbation (units of mb, negative values dashed). (b) Isotachs of horizontal velocity (m s^{-1}). :) Isotachs of vertical air motion (m s^{-1}). The bold solid contour denotes the outflow boundary −0.1°C potential temperature perturbation). (From Droegemeier and Wilhelmson, 1987. Reprinted 'ith permission from the American Meteorological Society.)

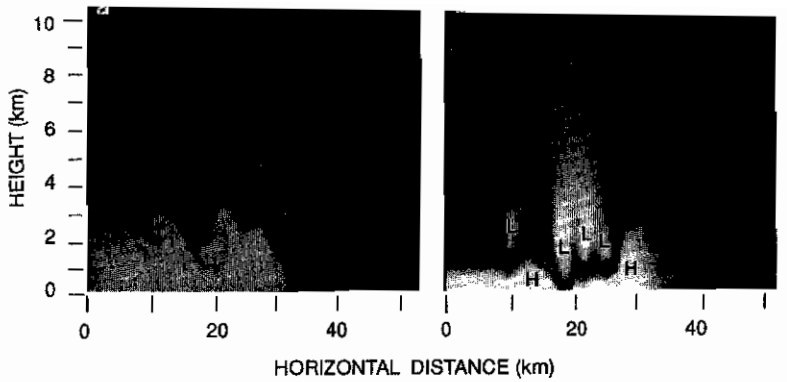

Figure 8.43 Numerical-model simulation of a thunderstorm outflow structure illustrating multiple wave structure atop the outflow: (a) Negative perturbation potential temperature (cold air) is shown by shading. The whiter the shading, the colder the air. (b) Perturbation pressure, with high (H) and low (L) anomalies indicated. (Results of Droegemeier and Wilhelmson, 1987, presented here in new graphical format by Kelvin Droegemeier.)

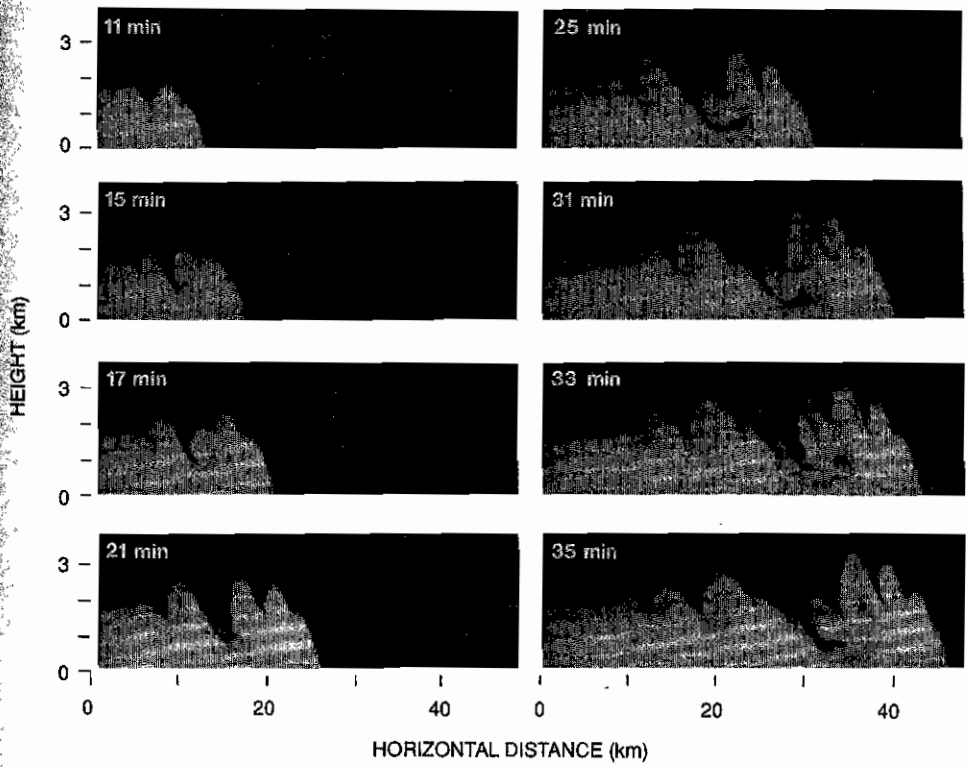

Figure 8.44 Numerical-model simulation of a thunderstorm outflow structure illustrating the sequence of wave generation on the top of the outflow layer. Negative perturbation potential temperature (cold air) is shown by shading. The whiter the shading, the colder the air. The lowest values, occurring near the surface, are about −5°C. (Results of Droegemeier and Wilhelmson, 1987, presented here in new graphical format by Kelvin Droegemeier.)

components of motion in Fig. 8.42b and c. Moreover, the pressure gradient surrounding the low in the x–z plane is in approximate cyclostrophic balance, such that

$$\frac{1}{\rho}\frac{\partial p}{\partial n} = \frac{V_s^2}{R_s} \tag{8.44}$$

where n is a coordinate normal to the streamlines and directed radially outward, R_s is the radius of curvature of a streamline, and V_s is the wind speed at a distance R_s from the center of the circulation. Equation (8.44) is a special case of (2.46) in which the axis of the vortex is horizontal. The data in Fig. 8.42 verify the balance. If the radius is taken to be 1 km, a representative value of V_s is 6 m s^{-1}. Thus, the term on the right is 0.36 m s^{-2}. The pressure field indicates the term on the left has a value of about 0.40 m s^{-2}. The minimum of pressure is thus dynamically induced in a manner similar to the pressure minima that characterize the vortices on the flanks of the supercell thunderstorm circulation [Sec. 8.5, Eq. (8.6), Fig. 8.20] or in the center of the tornado vortex [Sec. 8.8, Eq. (8.24)]. It can be further verified from the numerical simulation that the strong horizontal vorticity of the overturning in the head is generated by the horizontal gradient of buoyancy across the gust front, as discussed in Sec. 7.4.2 and Sec. 8.6.

From the model-calculated perturbation fields of potential temperature and pressure presented in Fig. 8.43, it can be seen that each of the waves in the upper boundary of the outflow is characterized by an overturning cyclostrophic pressure perturbation similar to that in the head. The Richardson number Ri indicated by the model fields is about 0.2, which, according to (2.170), is in the range of Kelvin–Helmholtz instability. The waves evidently are Kelvin–Helmholtz "billows" of the type illustrated in Figs. 2.4–2.8. Each originates in the head and propagates rearward, gradually damping and dissipating, while a new circulation forms in the head as a result of baroclinic generation. The sequence of wave generation is illustrated by the model-simulated cold pool evolution in Fig. 8.44.

The above numerical simulations illustrate the dynamics of the mature thunderstorm outflow. However, they do not treat the life cycle of the gust front. An empirical model of the life cycle of a thunderstorm outflow has, however, been synthesized from Doppler radar and other sources of information (Fig. 8.45).[232] The overturning head is again seen as a prominent feature. Stages II and III correspond to the mature phase illustrated by the numerical-model simulations. Later, in Stage IV, the overturning head separates and can propagate far away from the parent storm. As the gust front moves away it can trigger new cumulus or cumulonimbus. Satellite studies[233] show that these lines, which have separated from the parent storm, can maintain their identities as arc-shaped lines of cumulus clouds for several hours after the storms that produced the downdrafts have dissipated and can trigger new deep convective development up to 200 km from the location of the original storm. New deep convective developments are particularly favored where propagating arc lines intersect each other or where an arc line encounters pre-existing convection.

[232] This model was developed by Wakimoto (1982).

[233] Purdom (1973, 1979), Purdom and Marcus (1982), and Sinclair and Purdom (1982).

8.10 Downbursts

8.10.1 Definitions and Descriptive Models

We have seen that the downdraft is a salient feature of the thunderstorm circulation. Sometimes the downdraft becomes locally very intense over a short period of time, in which case it is referred to as a *downburst*. The following definitions are used to describe the phenomenon:[234]

Downburst—An area of strong winds produced by a downdraft over an area from <1 to 10 km in horizontal dimension.

Macroburst—A downburst that occurs over an area >4 km in dimension and is typically 5–30 min in duration.

Microburst—A downburst that covers an area <4 km in dimension and lasts 2–5 min. Differential velocity across the divergence center is >10 m s^{-1}.

Wet microburst—A microburst associated with >0.25 mm of rain or a radar echo >35 dBZ in intensity.

Dry microburst—A microburst associated with <0.25 mm of rain or a radar echo <35 dBZ in intensity.

The most scientific and public attention has been focused on the microburst, largely because of the danger it poses for aircraft operations. The existence and importance of this phenomenon were noted by Professor T. Fujita[235] in his investigations of aircraft accidents and patterns of damage to crops and property by violent winds that could not be explained by the vortical circulation patterns of tornadoes. In contrast to tornadoes, downbursts produce patterns that reflect strongly divergent and diffluent air motions at the ground. From surveying such damage patterns, Fujita was led to hypothesize the air motion pattern in a microburst shown in Fig. 8.46. As can be seen from Fig. 8.47 and Fig. 8.48, this conceptual model has proven accurate under scrutiny by Doppler radar observations and numerical modeling. Besides a shaft of strong downward velocity at its center, the microburst is characterized when it hits the ground by strong divergence at its center and an accelerating outburst of strong winds in a vigorously overturning gust-front head propagating more or less symmetrically away from the center of the microburst. When the microburst contains rain, dust, or other material from the surface, it can be seen visually (Fig. 8.49). Fujita conceptualized

[234] These definitions are based on the somewhat varying definitions used by Fujita (1985), Fujita and Wakimoto (1983), and Wilson *et al.* (1984).

[235] Professor T. Fujita, through his dogged and enthusiastic observations of storms and storm damage, is largely responsible for raising scientific and public consciousness about the downburst. He coined and promoted the terminology "downburst" and "microburst." Many of his investigations and adventures in the pursuit of this subject are described in his two books *The Downburst: Microburst and Macroburst* (1985) and *DFW Microburst on August 2, 1985* (1986).

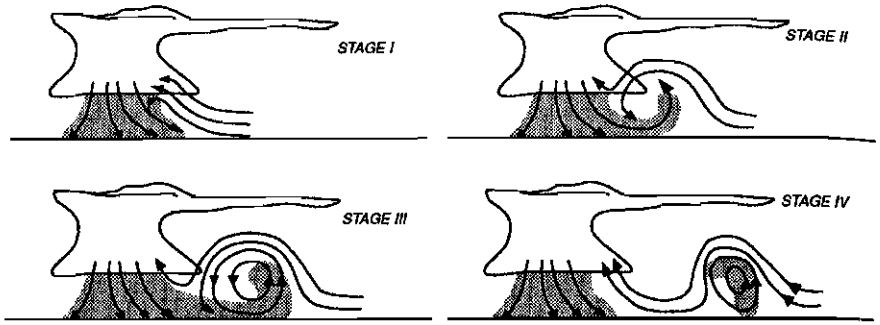

gure 8.45

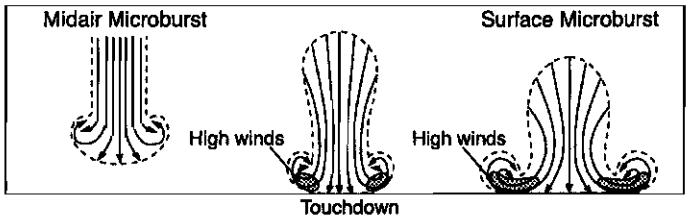

gure 8.46

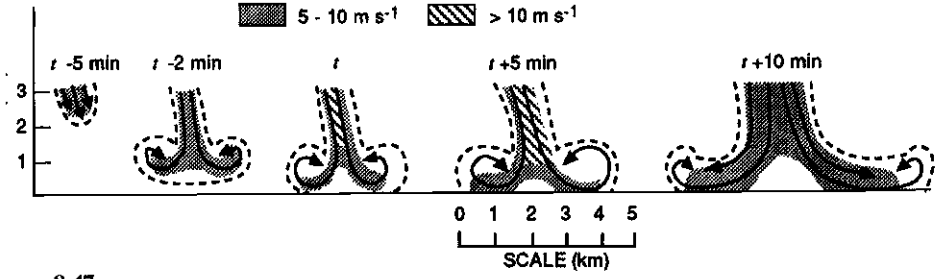

gure 8.47

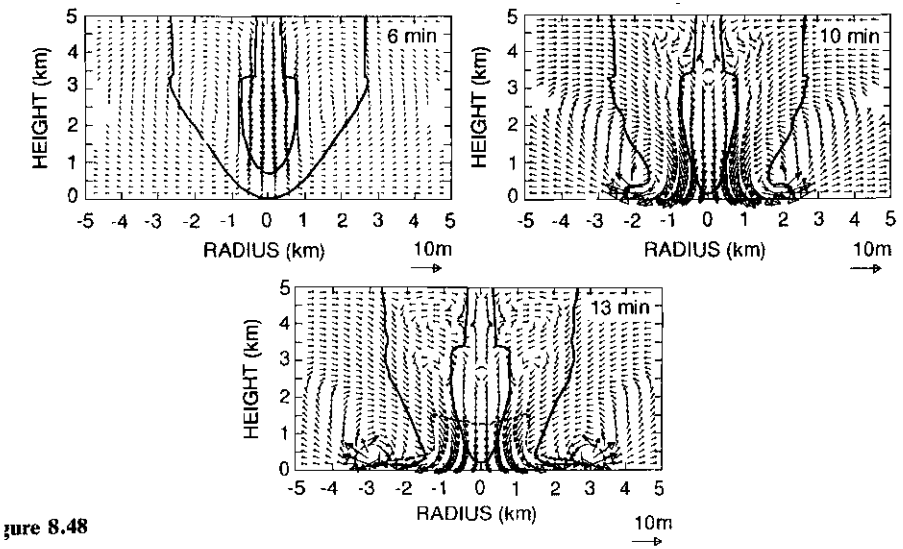

gure 8.48

the downburst in three dimensions, as illustrated in Fig. 8.50. These sketches illustrate the highly diffluent character of the surface wind and the expanding ring vortex formed by the circular gust-front head. The purpose of Fig. 8.50b is to show that some microbursts are associated with a small-scale cyclonic circulation aloft. This cyclonic vorticity is, however, largely weakened by divergence [i.e., the stretching term ζw_z in (2.59) is negative since $w_z < 0$] before parcels reach the ground.

8.10.2 Effects of Microbursts on Aircraft

Fujita's conceptual model has been used as an explanation for many aircraft accidents. A pilot must make quick critical adjustments in flying through the wind pattern of the microburst. For example, in taking off through a microburst (Fig. 8.51), the aircraft experiences an increase of headwind as it accelerates down the runway. Then, the aircraft lifts off in the increasing headwind and begins to climb (position 1). Near position 2, it encounters the microburst downdraft, and climb performance is decreased. By position 3, the headwind is lost. Consequently, airspeed is decreased, and lift and climb performance are further reduced. Added to this is the increased downdraft at the microburst center. By position 4, all available energy is needed to maintain flight, as the tailwind continues to increase. However, there is no source on which the aircraft can draw to increase its potential energy (climb). A large aircraft is typically configured ("trimmed") such that thrust, drag, lift, and weight are all in equilibrium. Thus, no pilot input is required for the aircraft to maintain a set trajectory. Since the airspeed is below the trim airspeed (decreasing lift and drag) at position 4, the airplane system will automatically respond so as to regain the equilibrium condition by pitching the nose downward. In the illustration, the pilot intervenes and compensates for this effect. Should the pilot not fully compensate, a more radical descent could occur. The descent rate continues to increase as the airplane passes through position 5. Depending on the strength of the event, encounter altitude, aircraft performance margin, and how quickly the pilot recognizes and reacts to the hazard, the high

Figure 8.45 Empirical model of the life cycle of a thunderstorm outflow. (From Wakimoto, 1982. Reprinted with permission from the American Meteorological Society.)

Figure 8.46 Conceptual model of a microburst hypothesized to explain ground-damage patterns. Three stages of development are shown. A midair microburst may or may not descend to the surface. If it does, the outburst winds develop immediately after its touchdown. (From Fujita, 1985.)

Figure 8.47 Empirical model of a microburst based on Doppler radar observations. Time t refers to the arrival of divergent outflow at the surface. Shading denotes wind speed. (From Wilson *et al.*, 1984. Reprinted with permission from the American Meteorological Society.)

Figure 8.48 Numerical-model simulation of a microburst at 6, 10, and 13 min after the initial model time. Thick lines represent the 10 and 60 dBZ radar reflectivity contours (i.e., the precipitation field). Dashed line encloses the area with temperature departures from ambient of less than −1 K. (From Proctor, 1988. Reprinted with permission from the American Meteorological Society.)

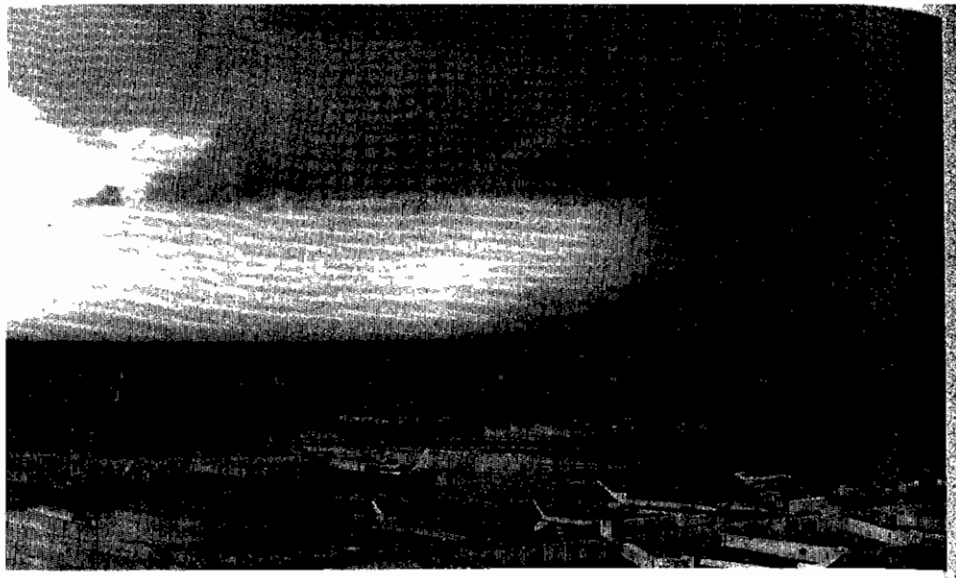

Figure 8.49 Photo of a microburst at Stapleton Airport, Denver, Colorado. The structure of the microburst is made visible by precipitation, dust, and other material from the surface. (Photo courtesy of W. Schreiber-Abshire.)

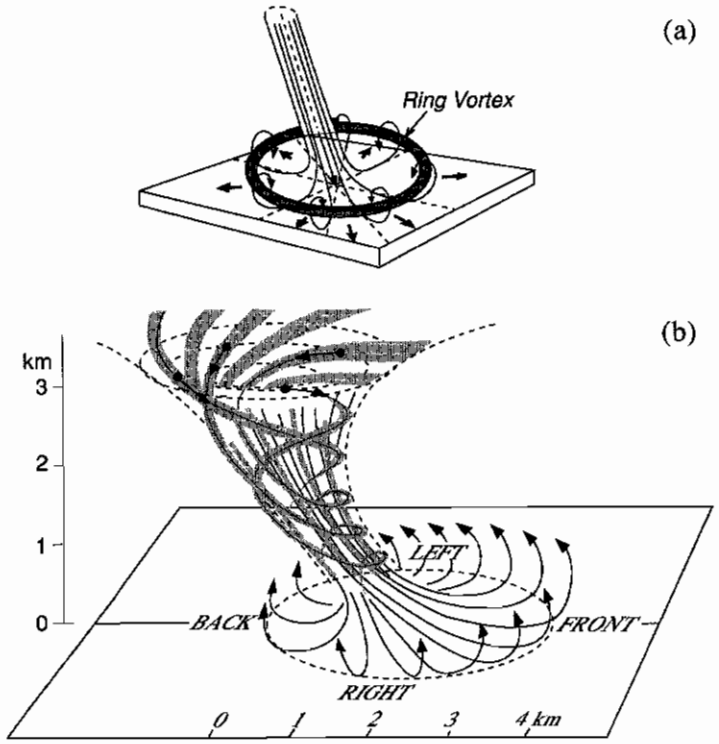

Figure 8.50 Three-dimensional visualization of a downburst. (a) Ring vortex at edge of gust front. (b) Rotation in the microburst. (From Fujita, 1985.)

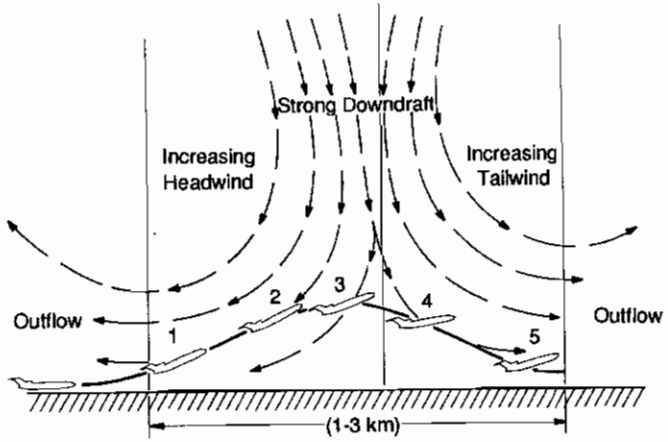

Figure 8.51 Idealization of an aircraft taking off through a microburst. After lifting off in an increasing headwind at 1, the aircraft begins to lose the headwind and enter the downdraft at 2, experiences stronger headwind loss at 3 with subsequent arrest of climb, begins descending in increasing tailwind at 4, and experiences an accelerating descent rate through 5. (From Elmore *et al.*, 1986. Reprinted with permission from the American Meteorological Society.)

descent rate may be impossible to arrest before the plane crashes into the ground.[236]

8.10.3 Dynamics of Microbursts

Investigations of the dynamics of microbursts have focused on two main issues. First, the mechanisms driving the downdraft have been sought. These mechanisms turn out to be primarily microphysical and thermodynamical. We will examine these mechanisms in Sec. 8.10.3.1. The second issue concerns the dynamics of the rotor circulation constituting the outward-propagating ring vortex, where the strong surface winds are located. We will examine the rotor dynamics in Sec. 8.10.3.2.

8.10.3.1 Mechanisms Driving Microbursts

The mechanisms of downdraft acceleration are approached through examination of the vertical component of the equation of motion (2.47), which in the absence of the frictional force may be written as

$$\frac{Dw}{Dt} = -\frac{1}{\rho_o}\frac{\partial p^*}{\partial z} + B\left(\theta_v^*, p^*, q_H\right) \tag{8.45}$$

where the dependence of the buoyancy B on the thermodynamic variables (θ_v^*, p^*, q_H) is given by (2.52). In a case study of downbursts observed by Doppler

[236] This illustration is taken from Elmore *et al.* (1986).

radar,[237] the terms on the right-hand side of (8.45) were estimated by performing thermodynamic retrieval analysis of the type discussed in Sec. 4.4.7.

The pressure gradient acceleration in (8.45) was found to be small compared to the buoyancy. This result could have been anticipated since the microburst is characterized by a pressure maximum at the surface, which produces an upward-directed pressure gradient force acting against the downdraft. The microburst problem thus reduces to understanding the negative contributions to B. Doppler radar data showed that the vertical acceleration [left-hand side of (8.45)] in the case study microburst was ~ 0.1 m s^{-2}. The precipitation mixing ratio implied by the observed radar reflectivity [Eq. (4.12)] suggested that only about 20% of the total acceleration was accounted for by precipitation drag [i.e., by the contribution of $-q_H$ to B in (2.52)]. If the contribution of p^* to B in (2.52) is small, then 80% of the negative buoyancy in the downburst must have been associated with θ_v^*. A value of $\theta_v^* = -2.5$ K is thus implied. This value is consistent with values of θ_v^* obtained by application of thermodynamic retrieval to the Doppler radar–derived flow field. If all the hydrometeors had been ice, melting could have accounted for only $\theta_v^* = -0.4$ K. Thus, most of the cooling responsible for the negative buoyancy of the downburst appears to have been brought on by evaporation of hydrometeors.

Radar evidence from other cases also suggests that microphysically induced negative buoyancy is crucial to microburst generation. However, it suggests that in some cases melting may be more important. In Fig. 8.52, dual-polarization radar measurements of the type discussed in Sec. 4.3 show a narrow region of near-zero differential reflectivity Z_{DR} [Eq. (4.25)] within the region of maximum reflectivity of the thunderstorm. This Z_{DR} hole indicates a narrow shaft of hail within the heavy shower of precipitation since, as illustrated by Fig. 4.2, the near-zero Z_{DR} is a signature of ice, while positive Z_{DR} is a signature of rain. This narrow hailshaft was coincident with the formation of a microburst, whose position was indicated by the diffluence of oppositely directed wind maxima at the surface (arrow in Fig. 8.52). Thus, we have circumstantial evidence that melting of hail was important to the dynamics of this microburst.

The observational results indicating that evaporation and melting are the key factors in producing downburst acceleration are reinforced by calculations with a one-dimensional, time-dependent nonhydrostatic model of the type described in Sec. 7.5.2.[238] The model domain is a cylinder of radius R with its top at 550 mb and its bottom at 850 mb. The bottom is open. At the top are assumed to be specified size distributions of rain and hail particles. An explicit microphysical scheme (Sec. 3.5) is used to predict the evolution of the particle distributions. The entrain-

[237] This outbreak of thunderstorms over Colorado containing several downbursts was documented in detail by Kessinger *et al.* (1988).

[238] This model was designed and used in two studies by Srivastava (1985, 1987). In the 1985 study, he performed calculations for downbursts containing only rain. The 1987 study extended the results to allow for the effects of hail as well as rain in a downburst. As well as being landmarks of insight into downdraft dynamics, these papers illustrate dramatically the usefulness of a simple one-dimensional model.

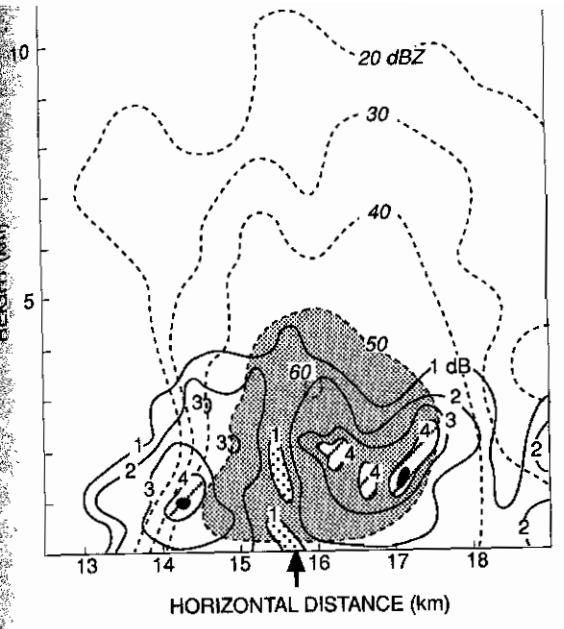

Figure 8.52 Vertical cross section showing dual-polarization Doppler radar measurements obtained in a thunderstorm in northern Alabama. Reflectivity data are presented in contours of dBZ. Differential reflectivity Z_{DR} are shown in dB units. Arrow indicates location of the center of a surface microburst. (From Wakimoto and Bringi, 1988. Reprinted with permission from the American Meteorological Society.)

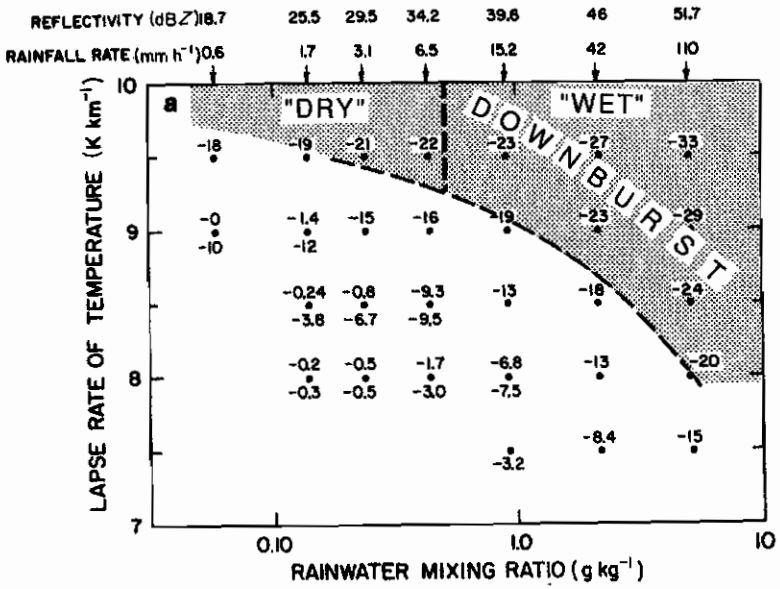

Figure 8.53 Results of a one-dimensional time-dependent nonhydrostatic cloud model of a downdraft. Plotted numbers are vertical air velocity (m s^{-1}) at a level 3.7 km below the top of the downdraft as a function of the lapse rate in the environment and total liquid water mixing ratio at the top of the downdraft. Numbers on top scale indicate the radar reflectivity and rain rate at the top of the downdraft. Curved dashed line separates downbursts (<20 m s^{-1}) from less intense downdrafts. Vertical dashed line separates dry (<35 dBZ) from wet (>35 dBZ) downbursts. Other conditions at the top of the downdraft are 550 mb, 0°C, and 100% relative humidity. The relative humidity of the environment is 70%, and there is no entrainment of environmental air. (Adapted from Srivastava, 1985. Reproduced with permission from the American Meteorological Society.)

ment rate is assumed to be inversely proportional to R [consistent with the continuous entrainment models considered in Sec 7.3.2, e.g., (7.38), (7.46), (7.48)]. The environmental lapse rate and humidity are specified. In calculations including only raindrops in the water-continuity equations, the microphysical and environmental conditions that produced downdrafts of >20 m s^{-1} in intensity were sought. Such a strong downdraft was taken to be an indication of a downburst. Results for the case of zero entrainment (achieved effectively at a radius of about 1 km) and an initial Marshall–Palmer distribution [Eq. (3.70)] of raindrops falling into the top of the domain are shown in Fig. 8.53. They indicate that downbursts are most readily obtained as the lapse rate approaches the dry adiabatic (9.8°C km^{-1}) and as the rainfall rate (or radar reflectivity) increases. Other results, not shown in the figure, are that the tendency toward downburst occurrence increases with decreasing mean raindrop size (since small drops evaporate more readily than large ones), with a *less* well-mixed boundary layer (in which relative humidity rather than mixing ratio is assumed constant in the environment) and with *increased* relative humidity in the environment. The last two results are somewhat counterintuitive, since microbursts often occur in dry and/or well-mixed boundary layers. However, the physics are clear. As the relative humidity (RH) of the environment is increased for a given temperature profile, especially near the top of the downdraft layer, buoyancy in the downdraft, measured relative to the environment, becomes more strongly negative [i.e., $q_v^* \equiv q_v - q_{ve}$ becomes more largely negative as RH increases since $q_v = q_{vs}(T)$, $q_{ve} = \mathrm{RH} \cdot q_{vs}(T_e)$, and $T < T_e$]. The optimal conditions for downburst formation in the absence of ice are then indicated to be an environment close to dry adiabatic, with a high rainwater content near cloud base and a minimum downdraft radius of 1 km. Note that there is no indication from these calculations as to why the downburst should be small in scale.

When hail as well as rain is included in the precipitation falling into the top of the model domain, calculations show that the additional negative buoyancy provided by melting can produce downbursts when the lapse rate is more stable than dry adiabatic. At higher environmental stability, higher precipitation content in the form of ice and relatively higher concentrations of small precipitation particles are required to generate an intense downdraft. At lower environmental stability, both dry and wet downbursts are possible. As the stability increases, only progressively wetter downbursts are possible. As the environment becomes even more stable, only wet downbursts having substantial precipitation in the form of ice are possible.

Numerical modeling of downbursts with a two-dimensional model of the type discussed in Sec. 7.5.3 is consistent with the one-dimensional model results just described. In the example examined here,[239] a bulk cold-cloud scheme (Sec. 3.6.2) is used to represent microphysical processes in the water-continuity equations. The model domain is 5 km deep and 10 km wide. Calculations are initiated by prescribing a distribution of hail at the top boundary. Again, melting and evaporation are both found to be important in driving the downdraft, with evaporation being the stronger effect. The two-dimensional model provides additional insight into the distribution of these processes in time and space. Melting is more important in the earlier stages, with evaporation becoming dominant later and at lower levels. It is also found that the downdraft is *induced* by precipitation drag with the evaporation and melting becoming dominant subsequent to the initiation.

[239] From Proctor (1988).

8.10.3.2 *Rotor Circulation and Outburst Winds*

The two-dimensional model also provides insight into the rotor circulation and outburst winds at the surface (Fig. 8.48). The outflow that develops is qualitatively very similar to that of thunderstorm downdraft outflows in general (Fig. 8.39). The microburst differs only in intensity, especially with the outburst of surface winds that occurs when the microburst hits the ground (Fig. 8.46 and Fig. 8.49). This behavior is seen in the two-dimensional model results in Fig. 8.54. As indicated in

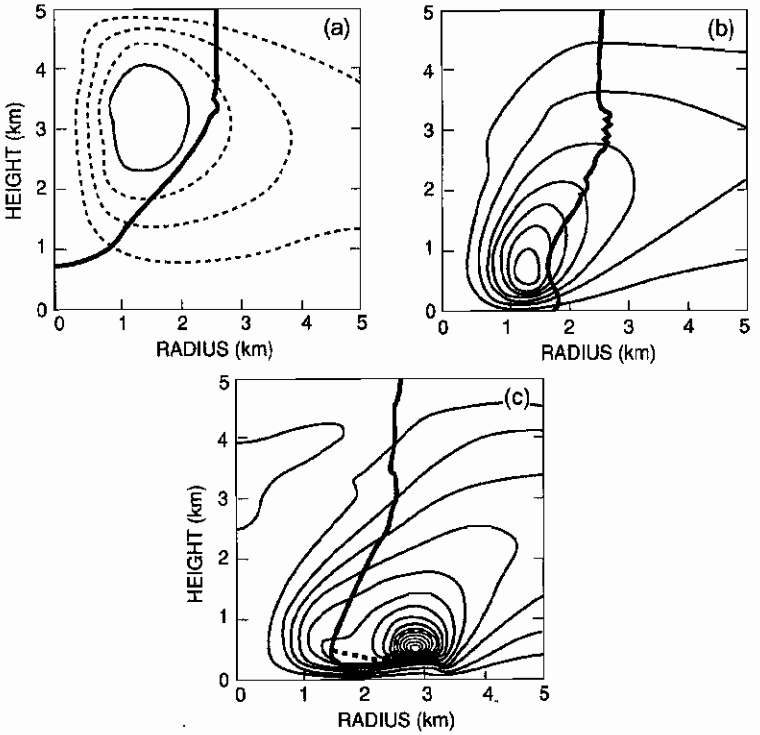

Figure 8.54 Results of a two-dimensional model showing the rotor circulation and outburst winds at the surface in a microburst. Radial–vertical cross sections for stream function for three successive times at intervals of 4 min. Thick solid line represents 10-dBZ radar reflectivity contour. The thick dashed line encloses area outside of precipitation shaft with temperature deviations from ambient of less than −1 K. The contour interval for the stream function is 8×10^5 kg s^{-1}, with intermediate contours dashed. (From Proctor, 1988. Reprinted with permission from the American Meteorological Society.)

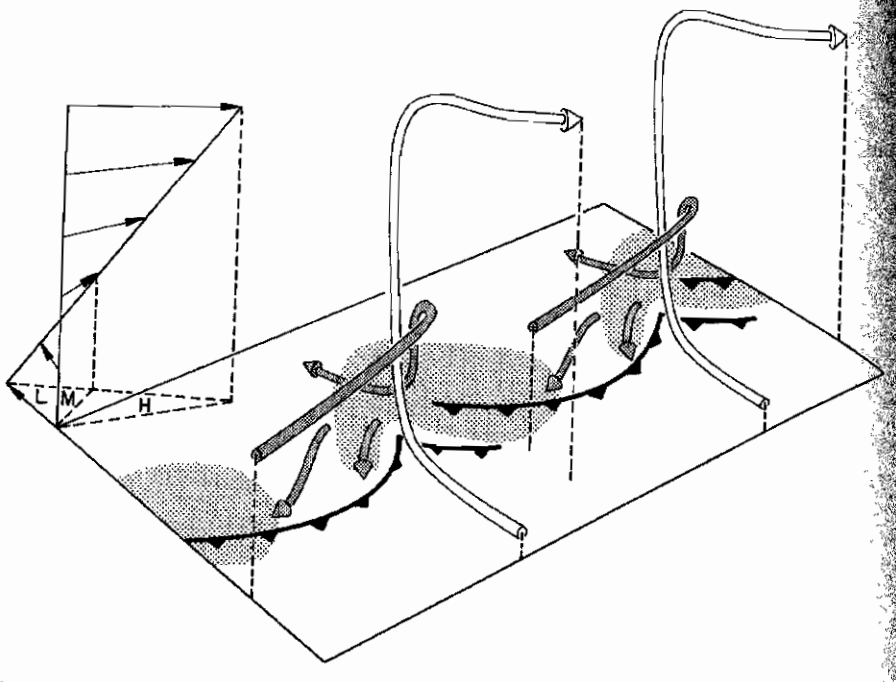

Figure 8.55

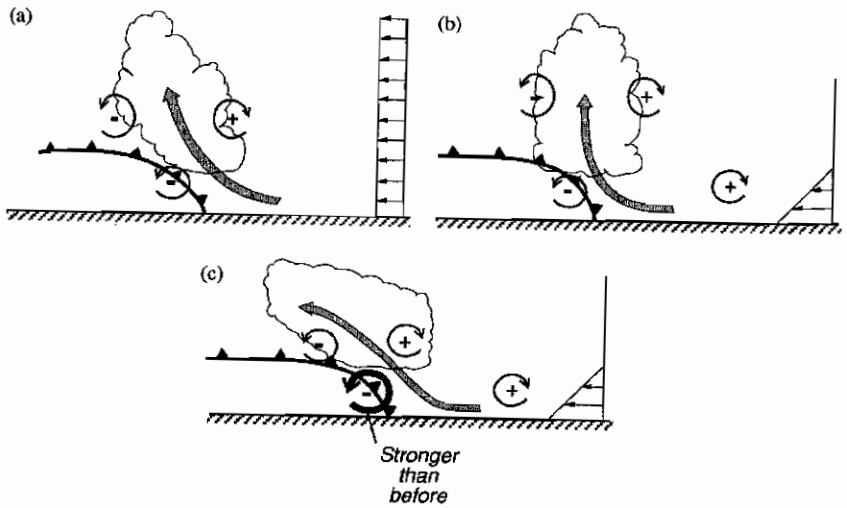

Figure 8.56

discussion of gust fronts (Secs. 7.4.2 and 8.9), the vortex in the outflow head is the result of the horizontal gradient of buoyancy across the edge of the outflow, as expressed by the baroclinic term B_x in the horizontal vorticity equation (2.61). The baroclinic generation is largest at the surface because the negative temperature anomaly in the downdraft is large only near the ground. The temperature anomaly above 1 km in height is less because the very rapid downward air motion warms the air adiabatically. Near the ground, where the downward motion is greatly slowed down, the evaporative cooling proceeds without compensating effects, thus producing a strong temperature contrast and strong baroclinic generation of circulation in the head. One result is the horizontal outburst of surface wind.

8.11 Lines of Thunderstorms

Up to now we have considered thunderstorms as individual entities. Often, however, thunderstorms occur in groups, and often in these groups the storms are distributed along horizontal lines—either straight or curved. Lines of thunderstorms can occur alone or as a part of a larger mesoscale convective system. In Chapter 9, we will consider lines of thunderstorms as components of larger storm systems. Here we look briefly into the environmental conditions required to maintain a line of thunderstorms, regardless of whether or not it is part of a larger system.

It is observed that a line of thunderstorms typically has a lifetime longer than that of the individual storms making up the line. Modeling studies[240] using two- and three-dimensional models of the type discussed in Sec. 7.5.3 have addressed the question of what environmental conditions promote such a long-lived line. Results point to the importance of the role of wind shear in the environment ahead of the line in sustaining the line's organization.

[240] Rotunno *et al.* (1988), Weisman *et al.* (1988), and Fovell and Ogura (1988, 1989).

Figure 8.55 Conceptual model of a line of supercell thunderstorms in an environment of deep, strong shear. Streamlines show flow relative to the individual storms composing the line. The environmental shear vector forms a 45° angle to the orientation of the line. The storms are arranged such that their circulations do not interfere. The shear profile on the left indicates the relative winds at low (L), middle (M), and high (H) levels. The stippled regions indicate the hook echo formed by the rain areas seen on radar. (As adapted from Lilly, 1979 by Rotunno *et al.*, 1988. Reprinted with permission from the American Meteorological Society.)

Figure 8.56 Heuristic diagram indicating horizontal vorticity (+ and −) in the vicinity of a long-lived line of multicell storms. Profile of horizontal wind component normal to the line is shown on the right of each panel. Frontal symbol marks outflow boundary. (a) Case in which there is no wind shear normal to the line in the environment. (b) Early stage of line development in case of low-level shear ahead of the gust front. (c) Late stage of line development in case of low-level shear ahead of the gust front. (Panels a and b from Rotunno *et al.*, 1988. Reprinted with permission from the American Meteorological Society.)